Alternative Nanostructures for Thermophones

Ali E. Aliev,*,† Nathanael K. Mayo,† Monica Jung de Andrade,† Raquel O. Robles,† Shaoli Fang,† Ray H. Baughman,† Mei Zhang,‡ Yongsheng Chen,§ Jae Ah Lee,⊥ and Seon Jeong Kim⊥

†A.G. MacDiarmid NanoTech Institute, University of Texas at Dallas, Richardson, Texas 75083, United States, ‡High-Performance Materials Institute, Florida State University, Tallahassee, Florida 32310, United States, §Institute of Polymer Chemistry, College of Chemistry, Nankai University, Tianjin 300071, China, and ⊥Center for Bio-Artificial Muscle and Department of Biomedical Engineering, Hanyang University, Seoul 133-791, South Korea

ABSTRACT Thermophones are highly promising for applications such as high-power SONAR arrays, flexible loudspeakers, and noise cancellation devices. So far, freestanding carbon nanotube aerogel sheets provide the most attractive performance as a thermoacoustic heat source. However, the limited accessibility of large-size freestanding carbon nanotube aerogel sheets and other even more exotic materials recently investigated hampers the field. We describe alternative materials for a thermoacoustic heat source with high-energy conversion efficiency, additional functionalities, environmentally friendly, and cost-effective production technologies. We discuss the thermoacoustic performance of alternative nanostructured materials and compare their spectral and power dependencies of sound pressure in air. We demonstrate that the heat capacity of aerogel-like nanostructures can be extracted by a thorough analysis of the sound pressure spectra. The study presented here focuses on engineering thermal gradients in the vicinity of nanostructures and subsequent heat dissipation processes from the interior of encapsulated thermoacoustic projectors. Applications of thermoacoustic projectors for high-power SONAR arrays, sound cancellation, and optimal thermal design, regarding enhanced energy conversion efficiency, are discussed.

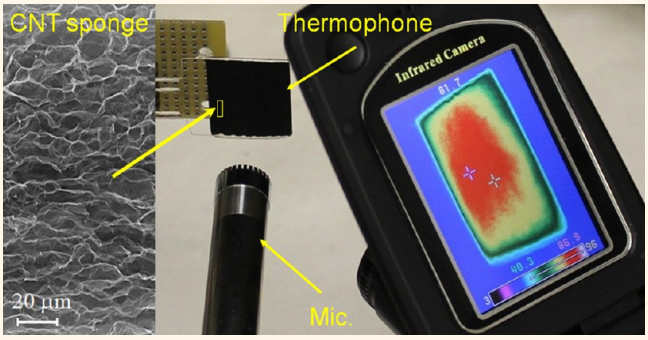

KEYWORDS: nanostructures · carbon nanotubes · thermoacoustics · sound · heat transfer

Thermoacoustic (TA) sound generation using nanostructured materials, like carbon nanotube (CNT) sheets, graphene films, and mechanically suspended metal nanowires has recently attracted much research interest because of possible practical importance. An efficient TA sound source requires a low heat capacity per surface area and efficient heat exchange with the surrounding medium. Among the studied materials (carbon nanotube,[1−6] graphene,[7,8] PEDOT:PSS[9] and ITO films,[10] porous silicon,[11] and metal nanowire arrays[12]), CNT aerogel sheets provide the highest efficiency. Table 1 compares the performance of some nanostructured materials applied as thermoacoustic heat sources. Indeed, the low heat capacity, high gravimetric mechanical strength, and extremely high accessible surface area make freestanding CNT sheets one of the best heat source materials for TA applications. The aerogel structure of freestanding CNT sheets makes the gas heating process volumetric rather than based merely upon the external surface. Moreover, high CNT alignment, resulting from CNT sheet fabrication during draw from a CNT forest, is another crucial feature that enhances the efficiency of sound generation; in randomly deposited CNTs or network of nanowires, the components aligned perpendicular to the current flow direction contribute little to sound production.

Transparent CNT aerogel sheets, which have the density of air and the gravimetric electrical conductivity of metals,[13] have been demonstrated to be suitable TA sources for use in harsh gaseous environments[1] and under water.[2] CNT films open to the propagation medium can generate smooth spectra sound over a wide frequency range ($1-10^5$ Hz). The variation of temperature and pressure in the vicinity of an open CNT heater induces sound wave propagation in the surrounding medium. Increasing the thermal gradient created between the surface of the CNT sheet and the surrounding medium within the thermal diffusion

* Address correspondence to ali.aliev@utdallas.edu.

Received for review December 14, 2014 and accepted March 7, 2015.

Published online March 08, 2015
10.1021/nn507117a

TABLE 1. Comparison of Recently Studied TA Sound Source Performances at the Frequency Most Sensitive to the Human Ear, f = 3 kHz

	heater material[a]	p_{rms}[b] (Pa)	SPL[b] (dB)	η[c] (%)	refs
1	CNT sheet (25.0 cm^2)	0.117	75	1.7×10^{-5}	single-layer freestanding MWNT sheet, D = 10 nm[4]
2	graphene, #1 (2.25 cm^2)	0.0045	47		three-layer graphene suspended on
	#2 (6.25 cm^2)	0.0028	43		80% porous PDMS[8]
3	graphene (1.0 cm^2)	0.0115	55	10^{-6}	20 nm thick graphene film on paper[7]
4	PEDOT:PSS	0.0025	32	10^{-6}	100 nm PEDOT:PSS film on glass substrate[9]
5	ITO film	0.0028	34	2×10^{-8}	100 nm ITO film on PET substrate[12]
6	Al film on porous silicon,	0.00235	57		30 nm thin Al film on 10 μm thick
	P_h = 1 W cm^{-2} (6.25 cm^2)		41		nanoporous (70%) silicon[10]
7	Au film on porous polymeric substrate (~10 cm^2)	0.034	64		40 nm thin Au film on 14 μm thick porous (5%) hydrogel substrate[14]
8	Al film on polyimide substrate (4 cm^2)	0.0019	39.5		40 nm Al film on 75 μm polyimide substrate[15]
9	suspended metal wire array (17.5 cm^2)	0.035	65		3 μm wide and 30 nm thick Al nanowires[11]

[a] The numbers in parentheses in the first column are the external surface area of the tested samples. [b] The sound pressure (p_{rms}) and sound pressure level (SPL re 20 Pa) were normalized to f = 3 kHz, P_h = 1 W, and r = 3 cm by assuming linear dependencies of $p(f)$, $p(1/r)$, and $p(P_h)$ and using data plots presented in the references. [c] The energy conversion efficiency η for the CNT aerogel sheet is shown for P_h = 1 W, while the P_h for other listed η values are provided in the indicated references.

length ($l_d = (2\alpha/\omega)^{1/2}$, where α is the thermal diffusivity and ω is the angular frequency of temperature modulation) results in increased sound pressure intensity. A higher applied power P_h produces an increased temperature gradient (eq 12 in ref 4) and subsequently higher sound pressure and Carnot's efficiency. Despite the extremely low heat capacity of CNT aerogel sheets, the low but finite heat capacity of air accompanied by its low thermal conductivity leads to an accumulation of heat in the vicinity of the heater. This elevated background temperature decreases the efficiency of the TA projector. The heat dissipation conditions are more severe for low-surface-area graphene and other continuous 2D films, like PEDOT:PSS, ITO films, and metallic thin films on the surface of porous materials, which results in degraded performance.

Complete characterization of the thermodynamic properties of suitable nanostructured materials for TA transductions is challenging and requires sophisticated methods and apparatus: a thermal atomic force microscope, the 3-omega self-heating method, suspended microfabricated devices, micro-Raman, and so on. However, the slope of sound pressure plotted *versus* frequency and applied ac power can explicitly characterize heat source performance.

We address here the thermal, acoustical, and energy conversion issues in TA projectors by seeking alternative heat source materials that provide additional functionality, are environmentally friendly, and can be made using cost-effective production technologies. We systematically investigate the spectral and applied ac power responses for materials with different thicknesses, porosities, and heat capacities and analyze the effects of heat accumulation on the fundamental efficiency of TA sound generation.

RESULTS

For the frequency region f < 100 kHz, the linear amplitude−frequency response of a TA device results from the negligible heat capacity of the nanostructured heat source, C_h[1,4]

$$p_{rms} = \frac{f}{2\sqrt{2}C_p T_0} \cdot \frac{1}{r} \cdot P_h \quad (1)$$

where C_p is the heat capacity of the gas, T_0 is the temperature of the surrounding gas, r is the distance to the microphone, and P_h is the power applied to the heat source. This dependency has been demonstrated for freestanding CNT sheets, both single-walled and multiwalled. For heat source structures with larger diameter constituent fibers, flakes, or films, the heat capacity of the heater should be taken into account. The corresponding slope of sound pressure *versus* frequency[16] for a thermally inert TA heat source gradually declines toward $p_{rms} \sim f^{0.5}$:

$$p_{rms} = \left[\frac{\sqrt{\alpha}\rho_0}{2\sqrt{\pi}T_0 C_h^*}\right]\frac{\sqrt{f}}{r} P_h \quad (2)$$

where $C_h^* = C_h \times \rho_h \times h$ is the heat capacity per unit area of the heat source, with density ρ_h, and thickness h, α is the thermal diffusivity of gas, and ρ_0 is the gas density. The full range of frequency dependencies (n in $p_{rms} \propto f^n$) as a function of C_h/C_p can be found from the general solution for spherical TA radiation:[4]

$$p_{rms} = \frac{i\rho_0\omega^2 a^2}{\sqrt{2}k_1 T_0(i4\pi a^2\omega C_h + i4\pi a^2 k_1 \kappa)} \cdot \frac{1}{r} \cdot P_h$$
$$= \frac{f}{2\sqrt{2}T_0\left(\frac{\rho_h h}{\rho_0} \cdot \sqrt{\frac{\pi f}{\alpha}} \cdot C_h + C_p\right)} \cdot \frac{1}{r} \cdot P_h \quad (3)$$

where a is the radius of the TA pulsating spherical heater, $\omega = 2\pi f$ is the angular output frequency, $k_1^2 = \omega/2\alpha$ is the real part of thermal wavenumber, and κ is the thermal conductivity of the surrounding gas. Similar equations have been derived for various boundary conditions using different approaches.[1,6,17]

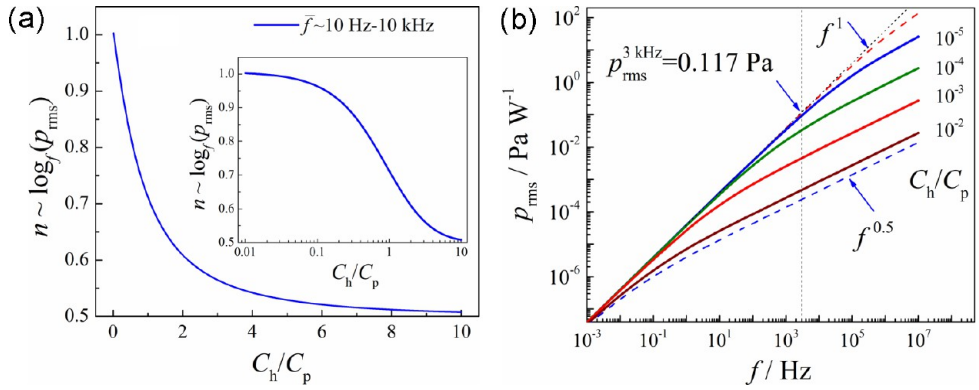

Figure 1. (a) Power factor *n* of sound pressure slope ($p_{rms} \propto f^n$) *versus* heat capacity ratio, C_h/C_p, numerically simulated using MatLab by fitting $p_{rms} = Af^n + B$. The inset shows a development of power factor from 1 to 0.5 on a logarithmic scale. (b) Output frequency dependence of sound pressure for different C_h/C_p plotted using eq 3.

Figure 1a shows the numerically derived dependence of sound pressure slope, $n \approx \log_f(p_{rms})$, on the heat capacity ratio, C_h/C_p. The experimental parameters used for this graphical simulation of eq 3 are P_h = 1 W, r = 3 cm, T_0 = 300 K, and h = 18 μm and, for open ambient air, ρ_0 = 1.184 kg m^{-3}, C_p = 1006.3 J kg^{-1} K^{-1}, and α = 22 mm^2 s^{-1}. The frequency exponent n in Figure 1a was averaged over a wide frequency range, 10 Hz to 10 kHz, for each given C_h/C_p. Figure 1b shows the dependence of sound pressure on frequency for increasing C_h/C_p. It gives precise crossover between two regimes with dominated C_p ($p_{rms} \propto f^1$) and dominated C_h ($p_{rms} \propto f^{0.5}$). The dotted vertical line at 3 kHz indicates the control values of sound pressure, which we frequently use in the following discussion. The blue dashed curve right below $C_h/C_p = 10^{-2}$ corresponds to the close-packed multiwalled carbon nanotube (MWNT) structure (ideal hexagonally packed structure of MWNTs with van der Waals spacing (0.34 nm) between individual nanotubes), whereas the red dashed curve right above $C_h/C_p = 10^{-5}$ corresponds to the aerogel density, freestanding MWNT sheet. Note the factor of 400 between the top and bottom dashed curves is consistent with the densification factor: the ratio of initial thickness of the CNT aerogel sheet ($h \sim 18\ \mu$m) to the sheet thickness obtained when the aerogel sheet collapses to a dense carbon nanotube film, $h \sim 45$ nm (after densification by wetting with volatile alcohol and subsequent drying).[13] All of the carbonaceous structures studied fell within the C_h/C_p region between these two dashed curves.

The thickness of the heater h and the heat exchange efficiency also affects the slopes of sound pressure *versus* frequency and *versus* applied ac power (see supporting materials of ref 4). Hence, one can make certain conclusions on the structural nature of the TA heater from the $p_{rms}(f)$ and $p_{rms}(P_h)$ obtained at different frequencies. Below, the performance of TA devices based on different nanostructured materials is studied using the slopes for $p_{rms}(f)$ and $p_{rms}(P_h)$. Very important additional information on heat exchange and accumulation can be extracted by monitoring the temperature on the surface of the heater.[18]

Improving structural homogeneity, reducing heat capacity, and enhancing the heat exchange coefficient with the surrounding gas for new nanostructured heat sources are the major challenges for boosting the temperature modulation gradient, which governs efficiency. The bundling of individual CNTs into large ropes (containing 50−100 nanotubes) creates dramatic current redistribution in the CNT sheet; current flows mainly through the bundles. Only a small fraction (<10%) of nanotubes on the surface of those bundles can effectively interact with surrounding gas and contribute to the heat exchange process. Nanotubes in small bundles and single nanotubes are at much lower temperatures due to a higher thermal exchange efficiency (resulting from the high surface-to-volume ratio and lower heat capacitance). The thermal inertia of large bundles increases the average temperature of the surrounding gas and decreases the overall efficiency of the Carnot cycle. Thus, our search is for new heat sources that adopt the small heat capacity and high surface area of freestanding CNTs, while being less susceptible to bundling by van der Waals forces than are CNTs.

A nanostructured heat source having a positive temperature coefficient of resistivity (TCR) will be explored to realize a desired dynamic redistribution of current pathways. To achieve metallic conductivity with a positive TCR, we evaluated metal-coated polymer fibers having diameters above 30 nm to avoid the severe bundling usually observed for nanotubes and nanofibers having diameters below ~30 nm.

Freestanding CVD-Grown MWNT Forest. The thermoacoustic and photoacoustic response of forests of as-grown, aligned MWNTs suffers from heat transfer from the heated MWNT layer to the silicon growth substrate. This heat loss to the substrate, which is especially pronounced for short forests, results in low efficiency and a sharp frequency dependence of the sound pressure, $f^{1.2}$.[19] Here we test the TA sound generation ability of a freestanding CVD-grown MWNT forest peeled from

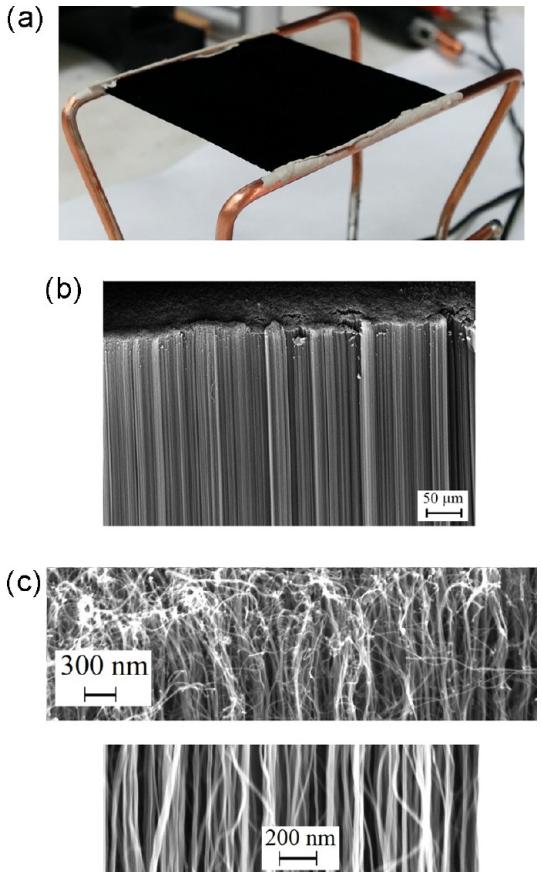

Figure 2. (a) Picture of a 250 μm tall (3.5 × 3.5 cm^2) F-MWNT-F attached to parallel copper wire electrodes by silver paste. (b) Scanning electron microscope (SEM) image of the forest's sidewall. (c) Higher magnification SEM images of the forest sidewall: the top panel is for a top layer, and the bottom panel is for a middle part of the forest.

the silicon growth substrate as a whole sheet (3.5 × 3.5 cm^2). It is well-known that the porosity of a CVD-grown forest is extremely high, V_{void}/V_{CNT} > 99%, and nanotubes in the forest are less bundled than in the MWNT aerogel sheets fabricated by drawing from a forest.

The 250 μm tall freestanding MWNT forest (F-MWNT-F), shown in Figure 2a, has a stable 120 Ω resistance after repeated current cycling (the initial resistance was 132 Ω). While the 250 μm and taller drawable forests can be easily detached from the silicon substrate by pulling the sheet under elevated angles, the short nondrawable forest (h < 100 μm) requires an additional heat treatment (oxidation of metallic catalytic nanoparticles in air at 450 °C for 30 min) to reduce the forest−substrate coupling. Note, the diameter of individual MWNTs in all three nanostructures mentioned in this paper (freestanding MWNT sheet, freestanding MWNT forest, and MWNT sponge) is 10 ± 1 nm. The heat capacity of as-grown and densified forest samples was measured using the heat capacity option of a physical property measurement system (Quantum Design Inc.) in the temperature range of 2−300 K and a differential scanning calorimeter Q2000 (TA Instruments Inc.) in the temperature range of 250−600 K. The measured heat capacity for the freestanding forest shows temperature dependence similar to that of graphite and a room temperature value of 700−750 J kg^{-1} K^{-1} (see Figure S2 in Supporting Information). Therefore, for the below carbon structures, we have used the accepted value for graphite (C_p = 716 J kg^{-1} K^{-1}).

In the low-frequency region, f < 20 kHz, the forest exhibits a linear sound pressure spectrum as predicted by eq 1 for a nanostructured source having negligible heat capacity. Using the specific heat capacity of air, C_p = 1006 J kg^{-1} K^{-1}, and a microphone distance of 3 cm, the pressure variation slope obtained using eq 1 is shown in Figure 3a as a green dashed line (with control point at p_{rms} = 0.117 Pa W^{-1} for f = 3 kHz). This line is consistent with the $p_{rms}(f)$ slope measured for the single freestanding MWNT sheet in wide (10 Hz to 140 kHz) frequency range (see Figure S1 in Supporting Information). However, since dynamic gas access to inner forest regions is restricted for the 250 μm tall forest, the correspondingly limited heat transfer coefficient β at increased power results in heat accumulation inside the forest. This heat accumulation produces an undesired increase in static background temperature, T_0, and a corresponding decrease in the TA sound pressure slope for both $p_{rms}(f)$ and $p_{rms}(P_h)$. The observed order-of-magnitude lower sound pressure, compared to that for the MWNT aerogel sheet, is a direct consequence of the increased heater thickness (h in eq 3) and reduced heat transfer ability from heater interior (reduced thermal diffusivity, α in eq 3).

For a low applied power (P_h = 3 W), the linear slope of $p_{rms} \sim f^1$ in Figure 3a is still conserved at low frequencies, indicating the negligible contribution of heat capacity of the forest compared to air. However, at higher frequencies, the $p_{rms}(f)$ slope is slightly decreased. The relatively low crossover between regimes with dominating C_p (f < 2 kHz) and dominating C_h (f > 2 kHz) is due to the thick and relatively dense structure of F-MWNT-F delaying heat dissipation from the interior at increased frequency. Increasing the forest thickness causes little change to the high-frequency slope (n = 0.9 for 80 μm and n = 0.86 for 250 μm thick F-MWNT-Fs at f = 3 kHz) but substantially reduces the absolute value of sound pressure. (Note, at f = 3 kHz, the thickness of both samples is larger than the thermal diffusion length of air, $l = (\alpha/\pi f)^{1/2}$ = 48 μm.) Perhaps, the applied ac current mostly flows through the top layer of the forest, which has an interwoven curled structure (see top panel of Figure 2c). Evidence suggesting this is provided by the similar electrical sheet resistance of 250 μm (120 Ω/□) and 80 μm (150 Ω/□) thick F-MWNT-Fs. Central and bottom parts of the forest, which have straight structures with few interconnections, play the role of heat pipes to the air.

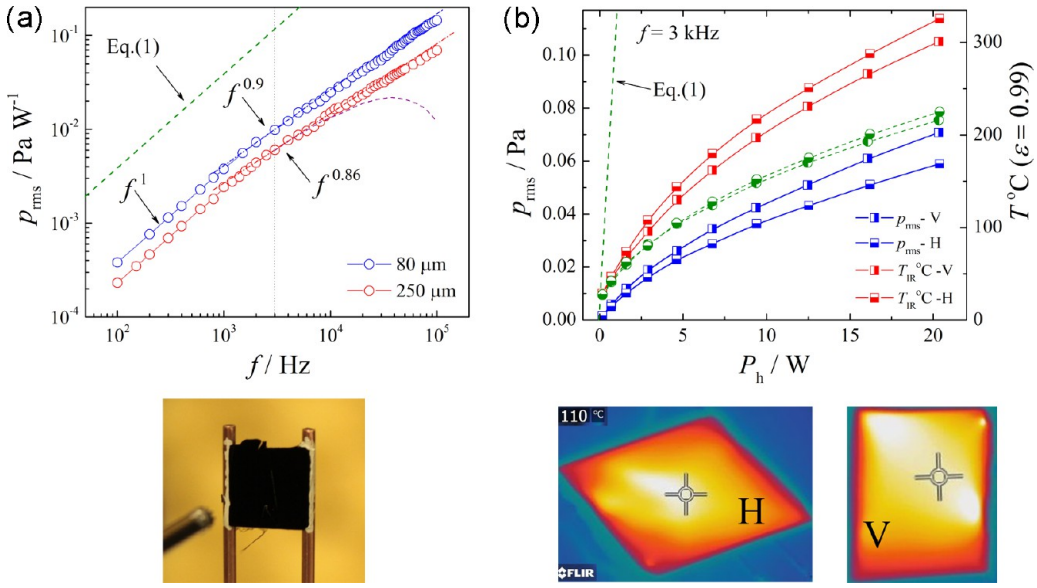

Figure 3. (a) Sound pressure spectra of F-MWNT-F measured at a distance of 3 cm in open air at T_0 = 25 °C. The sound pressures are normalized to the applied ac power, $P_h \sim 3$ W. The blue and red open circles show the $p_{rms}(f)$ response of 80 and 250 μm thick F-MWNT-F (1 × 1 cm^2), respectively. The purple dashed curve shows the deviation of $p_{rms}(f)$ from linear dependence for large (3.5 × 3.5 cm^2) F-MWNT-F shown in Figure 2a. The blue and red dash-dot lines behind both $p_{rms}(f)$ dependencies show the fitting lines for $f^{0.86}$ and $f^{0.88}$, respectively. The top green dashed line shows the theoretical line predicted by eq 1. Below the panel is shown a picture of a 1 × 1 cm^2 F-MWNT-F heater (80 μm) with a B&K 4138-A-015 microphone in front. (b) Sound pressure *versus* applied ac power (blue vertically half-filled squares are for vertically placed F-MWNT-F, and horizontally half-filled squares are for horizontally placed F-MWNT-F, respectively) measured at the distance of r = 3 cm for f = 3 kHz. The red half-filled squares show the temperature on the surface of the F-MWNT-F *versus* applied power (the alignment of the square filling is the same as for $p_{rms}(P_h)$) measured at the sample center using a FLIR T650sc infrared camera. The green half-filled circles show the temperature of F-MWNT-F measured by the resistance change method.[18] Images below panel (b) show the temperature profile for horizontally (H) and vertically (V) placed F-MWNT-Fs.

For large samples, one should take care of sound wave interference by reducing the measured sound pressure at both near- and far-field.[3] The $p_{rms}(f)$ dependencies in Figure 3a were measured for a 1 × 1 cm^2 F-MWNT-F using three different aperture microphones: a 12.5 mm ACO Pacific model 7046 (2−20 kHz, S = 54.3 mV/Pa), a 6.25 mm ACO Pacific model 7016 (5−120 kHz, S = 5.43 mV/Pa), and a 3.1 mm B&K pressure-field microphone 4138-A-015 (6−140 kHz, S = 0.543 mV/Pa). For a 3.5 × 3.5 cm^2 (h = 250 μm) F-MWNT-F, the destructive sound interference reduces the $p_{rms}(f)$ slope above 10 kHz (dashed purple curve) when the sound wavelength (λ_{10kHz} = 3.4 cm) becomes comparable to the sample dimension.

The deviation from a linear $p_{rms}(P_h)$ dependence in Figure 3b occurs at very low power, in contrast with the case of a single-layer MWNT aerogel sheet.[18] The temperature on the surface of the MWNT forest heater, measured using a FLIR 650sc infrared camera (FLIR Systems Inc.) with a preinstalled emissivity of 0.99, corresponding to a nearly perfect blackbody, strongly deviates from linear dependence on input power and provides a square-root dependence for an applied ac power above 5 W. To avoid sample degradation (the individual carbon nanotubes burn in air at T > 500 °C[20]), we restricted the applied power to give a maximum temperature on the surface of the heater of ∼300 °C.

The nonlinear behavior of $p_{rms}(P_h)$ and $T(P_h)$ in Figure 3b partially resulted from the nonlinear thermal conductivity of air in the vicinity of the heater ($\kappa \propto (T/M)^{1/2}$, for monatomic gases with molar weight M), which is enhanced at high power by blackbody radiation from the hot individual nanotubes. We observed the same behavior for a stack of multilayered MWNT sheets (n > 6).[18]

The heat exchange at high temperatures on the surface of nanoscaled heaters is accompanied by air convection. The temperature profile of horizontally (H) and vertically (V) placed F-MWNT-Fs, as measured by an IR camera, substantially differed from the aerogel-like porous structures of MWNT sheets. The temperature on the horizontally oriented F-MWNT-F is 30−40 °C higher than in the center of the vertically aligned sample (see Figure 3b at P_h = 20 W). While for the horizontally oriented sample the maximum temperature was observed in the center of the F-MWNT-F plate, for the vertically oriented sample, the maximum temperature is at the top of the plate (see thermal images in Figure 3b). The hot air layer in the vicinity of the heater increases the temperature background T_0 and reduces the sound pressure. Interestingly, the temperature of V- and H-oriented heaters measured by monitoring the resistance change[18] is much lower (∼100 °C) and does not show such a large difference (green half-filled circles in Figure 3b). Apparently, the

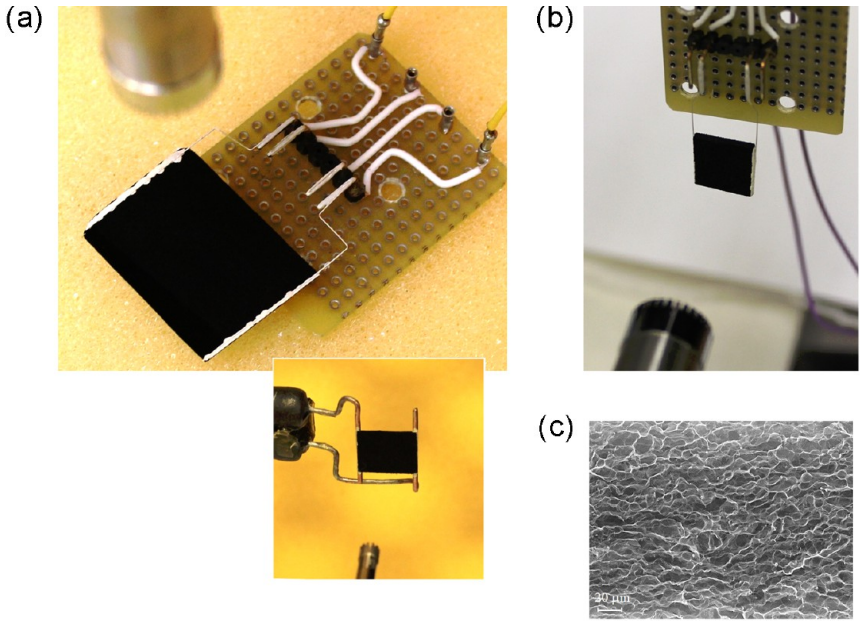

Figure 4. Pictures of the fabricated TA heat sources using (a) 2 × 2.5 cm^2 and (b) 1.5 × 1.5 cm^2 MWNT sponges with plate thicknesses of 100 and 200 μm, respectively. The inset to panel (a) shows a picture of the same 100 μm thick MWNT sponge reduced to 0.9 × 1.1 cm^2 to test the size-dependent interference effect. (c) SEM image of a sponge with a density of 30 mg cm^{-3}.

temperature of carbon nanotubes, which is determined by the applied ac current, is less affected by air flow outside of the forest than is the sound pressure created by the temperature gradient.

Highly Elastomeric MWNT Sponge. Developing flexible and deformable devices based on porous materials is of major interest in energy-related fields. Here, we demonstrate that carbon nanotube sponges consisting of highly porous conductive MWNT networks can serve as elastically compressible, flexible TA heat sources. Figure 4 shows two TA heat sources fabricated using 2 × 2.5 cm^2 (Figure 4a) and 1.5 × 1.5 cm^2 (Figure 4b) MWNT sponge films having thicknesses of 100 and 200 μm, respectively. With an electrical resistance of 16.4 and 8 Ω, the sponges can withstand several amps of electrical current along the sponge length direction in air.

The sponge fabrication process is simple and low-cost, utilizing poly(methyl methacrylate) (PMMA) microspheres as a template and poly(acrylonitrile) (PAN) as a precursor to create cross-links between MWNTs.[21] An assembly of PMMA microspheres is first coated with a mixture of MWNTs and PAN followed by pyrolysis which removes the PMMA and carbonizes the PAN. These sponges, whose densities vary from 10 to 36 mg cm^{-3}, have excellent mechanical properties and maintain stable mechanical performance during 1000 large-strain compression cycles. The porosity and the pore size of the MWNT sponges can be tuned easily by adjusting the concentration and particle size of the PMMA spheres. The MWNT sponges have a hierarchically porous structure, and the pore sizes range from several nanometers to tens of micrometers, as shown in Figure 4c.

The thin, partially transparent (h = 60 μm) MWNT sponge shows a linear slope of $p_{rms}(f)$ in the entire frequency range of the B&K 4138-A-015 microphone (6 Hz to 140 kHz). Like the freestanding MWNT forest, the thick MWNT sponge (100 μm) provides a lower slope of $p_{rms} \sim f^{0.75}$ in the audible and higher frequency region, which is typical for a TA heater that has a substantial heat capacity (Figure 5a). Note, decreasing the TA heater thickness from 100 to 60 μm resulted in an increased sound pressure from 0.0065 to 0.012 Pa, in accordance with eq 3. Apparently, the collapse of individual CNTs into large bundles (unavoidable in the solution-based sponge fabrication process) and the pyrolized PAN increase the volumetric heat capacity and thermal inertia of the sponge heater. However, the measured density (30 kg m^{-3}) and C_h*, comparable to the above self-supported MWNT forest, and an improved heat transfer to the ambient gas through large pores (~10−20 μm) resulted in better TA performance for the MWNT sponge. Even thinner films would be preferable to avoid heat accumulation, which is indicated by a deviation from a linear dependence of $p_{rms}(P_h)$ in Figure 5b. Increasing the heater surface area to 2 × 2.5 cm^2 introduces destructive interference, which decreases the sound pressure above 3 kHz (open blue circles in Figure 5a).

The easy to handle, flexible, and self-supporting MWNT sponge plates can be rolled into cylindrical (see inset to Figure 5b) or concave shapes to manipulate the sound wave. Bending the sponge multiple times (~100) about a curve with a radius of 5 mm did not affect the generated sound pressure within the measurement accuracy of 5%. These new results show that

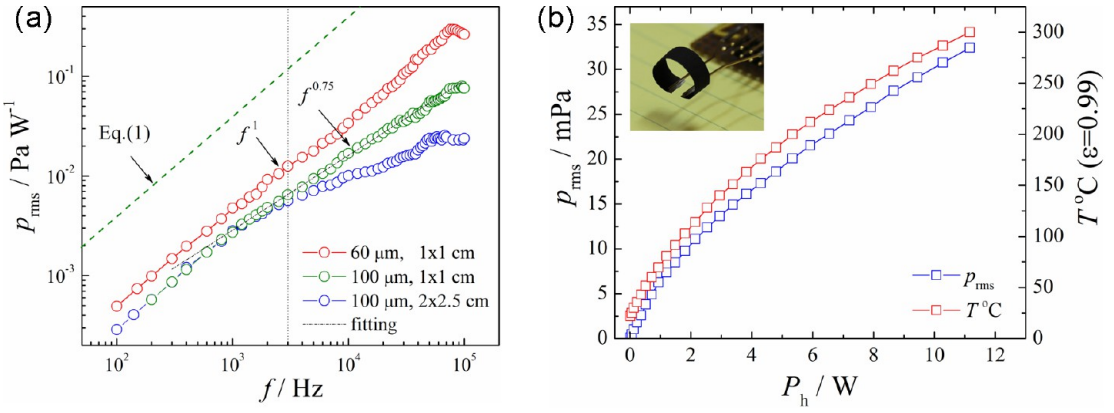

Figure 5. (a) Sound pressure spectra of 60 μm (1 × 1 cm^2), 100 μm (1 × 1 cm^2), and 100 μm (2 × 2.5 cm^2) thick MWNT sponges measured at a distance of 3 cm in air at T_0 = 25 °C. The sound pressure is normalized to the applied ac power, P_h = 0.56, 0.9, and 1.17 W, respectively. The green dashed line shows the theoretical line obtained using eq 1. (b) Sound pressure (blue open squares) *versus* applied ac power measured at a distance of 3 cm for f = 3 kHz. The red open squares show the temperature on the surface of MWNT sponge *versus* applied power measured using a FLIR T650sc infrared camera. The inset shows the bending ability of the 100 μm thick MWNT sponge strip rolled up into a ring.

carbon nanotube sponges could be used as mechanically robust elastically deformable TA sound transducers that now provide useful performance and have the potential for optimization in the future.

Highly Elastomeric Graphene Sponge. While the gravimetric surface area of a planar single-layer or few-layer graphene film is giant, the planar structure means that the possible total surface area per projector area is small. In order to avoid this problem, and at least partially utilize the high inherent properties of graphene (such as high electronic conductivity, thermal stability, and excellent mechanical strength), porous graphene materials including graphene nanomesh, crumpled graphene, and graphene foam have attracted considerable research interest.[22]

We here demonstrate the use of a high-surface-area, three-dimensionally (3D) nanostructured graphene sponge (GS) as a TA heat source. This essentially isotropic 3D cross-linked GS, which was fabricated by a solvothermal (ST) reaction in alcohol,[23,24] has air-like density and can be reversibly compressed to giant strains. Graphene oxide (GO) flakes were first ST assembled in ethanol to obtain a nearly homogeneous, ethanol-filled material. Following exchange of ethanol with water, the sponge was freeze-dried and then annealed under inert atmosphere at 400 °C to obtain the final GS. By varying the GO concentrations used for the ST reaction, GS possessing densities from 0.3 to 14 mg cm^{-3} were obtained, which in the former case have a much lower density than ambient air (1.2 mg cm^{-3}). The results discussed below are for GS having an uncompressed density of 2.75 mg cm^{-3}.

Thin slices of GS (shown in Figure 6) were taken by cutting along and perpendicular to the axis of the fabricated cylinders using a laser beam. The thermal conductivity of the GS, obtained as a product of density, heat capacity, and thermal diffusivity (measured using the angstrom method), $\lambda = \rho \times C_p \times \alpha = 0.016 \pm 0.002$ W m^{-1} K^{-1}, is 2 times lower than the thermal conductivity of air, 0.026 W m^{-1} K^{-1}. The fine microscopic structure of GS shows essentially isotropic heat conduction, that is, independent of the cutting direction ($\alpha_{||} = 2.25 \pm 0.1$ mm^2 s^{-1}, $\alpha_{\perp} = 2.31 \pm 0.1$ mm^2 s^{-1}). The heat capacity measured for densified samples shows wide variation (510−815 J kg^{-1} K^{-1}) depending on residual graphene oxide and organic contaminants.

To test the TA performance of the GS heaters, three samples were cut parallel (1.5 × 12.5 × 15 mm^3, 1 × 10 × 15 mm^3) and perpendicular (0.8 mm thick and 18 mm in diameter) to the cylinder axis. The obtained bulk resistances were relatively high: 475, 690, and 410 Ω, respectively. Despite their large thicknesses, the studied GS provided linear frequency dependencies of $p_{rms}(f)$ (see Figure 7a) close to the theoretical limit at low applied power, P_h < 0.5 W. The linear dependence of $p_{rms}(f)$ deviates little from n = 1 for thicker samples: n = 0.97 for h = 1 mm and n = 0.94 for h = 1.5 mm. This is consistent with the increase of C_h* in eq 3. However, further increase of P_h creates an accumulation of heat inside the GS voids, which causes a decline in the $p_{rms}(P_h)$ curve. This decline can be decreased, thereby increasing energy conversion efficiency, by using thinner GS plates as thermoacoustic heaters.

The high reversible compressibility and flexibility of sponge-type TA heaters is useful for fabrication of complex heater shapes and confined sound sources. To obtain optimal TA sound generation, the sponge thickness can be easily adjusted to the thermal diffusion length of the surrounding medium by laser cutting or by simply compressing the sponge plate.

Sheets of Gold-Coated Poly(acrylonitrile) Nanofibers. Since PAN is a strong, durable, and a high-melting carbon backbone polymer,[25] $(C_3H_3N)_n$, that can be easily electrospun, sheets of gold-coated PAN nanofibers were chosen for evaluation as TA sound projectors.

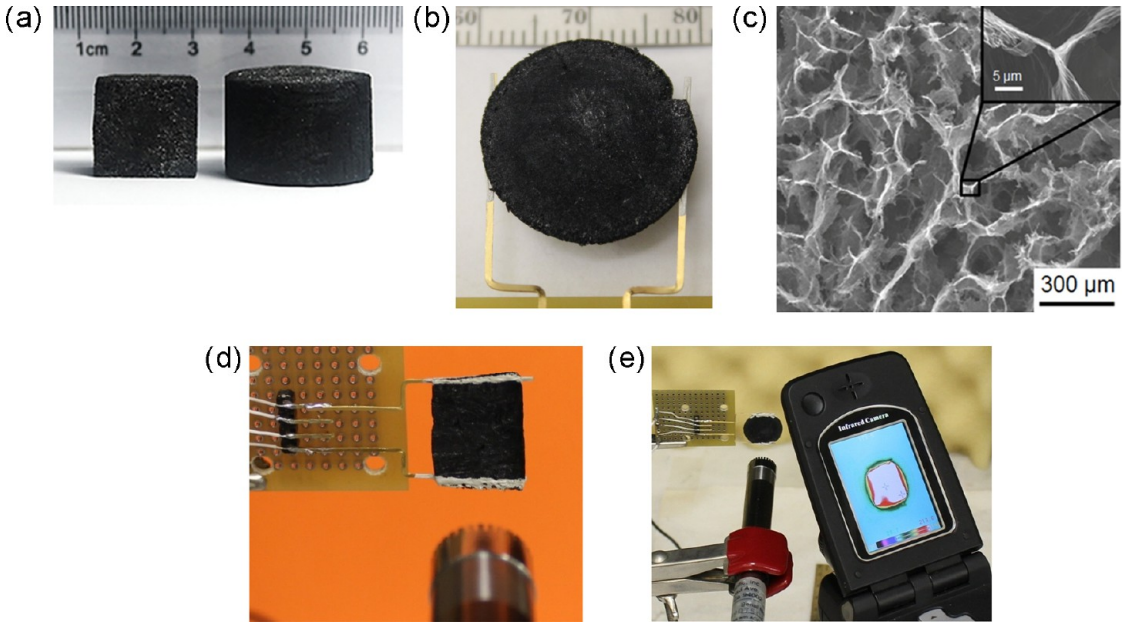

Figure 6. (a) GS cylinders fabricated by ST reaction. (b) An 0.8 mm thick GS plate, fabricated by laser cutting perpendicular to the cylinder axis, attached to gold-coated electrodes by silver paste. (c) SEM image of a GS with a density of 2.75 mg cm^{-3}. (d) A 1.5 mm thick GS plate cut parallel to the cylinder axis, placed 3 cm from a microphone (model 7046). (e) Infrared MobIR camera, with preinstalled emissivity of 0.99, shows the temperature on the surface of GS TA heater.

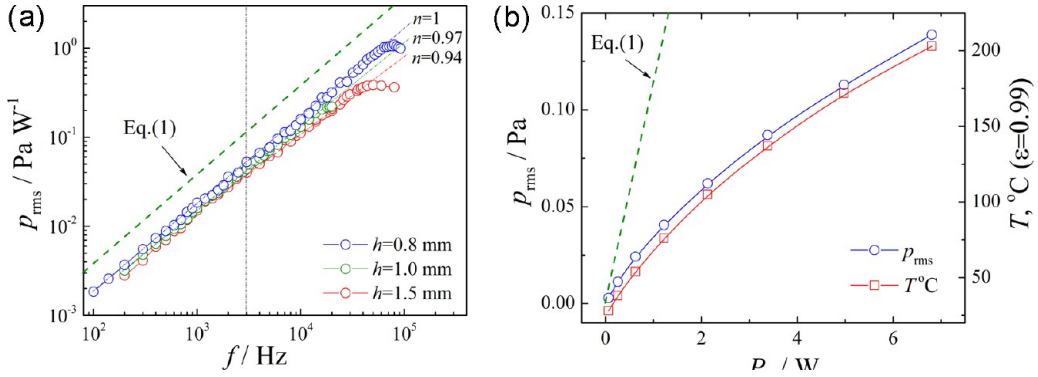

Figure 7. (a) Sound pressure spectra of 0.8 mm (open blue circles), 1 mm (open green circles), and 1.5 mm (open red circles) thick GS sponges measured at a distance of 3 cm in air at T_0 = 25 °C. The green dashed line shows the theoretical line predicted by eq 1. (b) Sound pressure *versus* applied ac power (open blue circles) measured at the distance of r = 3 cm, f = 3 kHz. The temperature of the GS (h = 0.8 mm, D = 18 mm) *versus* applied power (open red squares) was measured using a MobIR infrared camera (ε = 0.99).

The highly aligned electrospun PAN sheets shown in Figure 8a, with fiber diameters between 200 and 500 nm, are mechanically robust and can withstand relatively high temperatures in air (T_m = 317 °C). The diameter of individual fibers, the thickness of the PAN sheet, and its areal density can be easily controlled by proper choice of a precursor solution (presently 10 wt % of PAN, M_w = 150 000 in *N*,*N*-dimethylacetamide), applied voltage, distance between the spinning tip and two counter electrode pillars, and spinning time.[24]

The gold-coated nanofiber sheets (with electrical resistances of 532 and 16 Ω for low- and high-density PAN sheets, respectively) are optically transparent and mechanically robust, and the nanofibers do not form bundles. The gold coating was deposited as a 100 nm shell on each individual fiber by RF sputtering (DC/RF Reactive Magnetron Sputter, ATC Orion).

The low-density Au/PAN nanofiber aerogel sheet shown in Figure 8e provides high performance as a TA heat source in open air up to 100 kHz (see Figure 9a). The reduced slope of the dependence of sound pressure on output sound frequency, $p_{rms} \sim f^{0.8}$, starting at frequencies below 3 kHz, indicates the significant volumetric heat capacity of the sheet compared to the volumetric heat capacity of air. The sound pressure measurements at a short microphone distance (r = 1 cm) suffers with severe interference, as shown in Figure 9a by the open red square curve. Despite the high thermal inertia of large-diameter PAN fibers (400−600 nm), which decreases the overall performance of the TA heater, the open aerogel structure

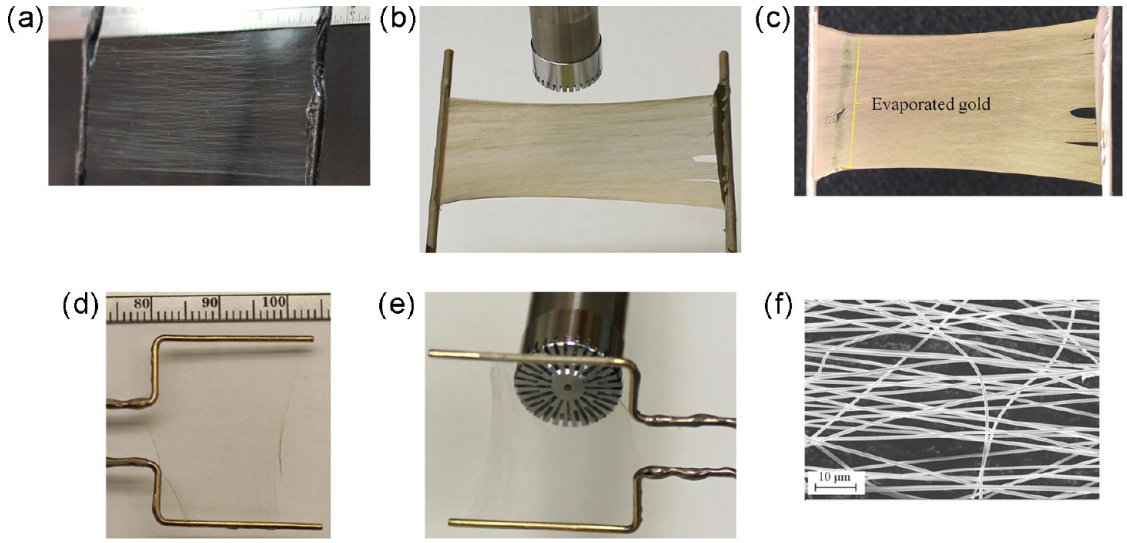

Figure 8. (a) Photograph of a highly aligned, transparent PAN fiber sheet between two carbon-coated metallic wires. (b) Gold-coated, high-areal-density PAN sheet (R = 16 Ω) placed 3 cm from a microphone. (c) Sheet of panel (b) after applying 0.7 A current. Low-areal-density PAN sheets before (d) and after (e) gold coating. The Au PAN sheet had a R = 532 Ω resistance and an optical transparency >95%. (f) SEM image of the gold-coated PAN sheet of (e).

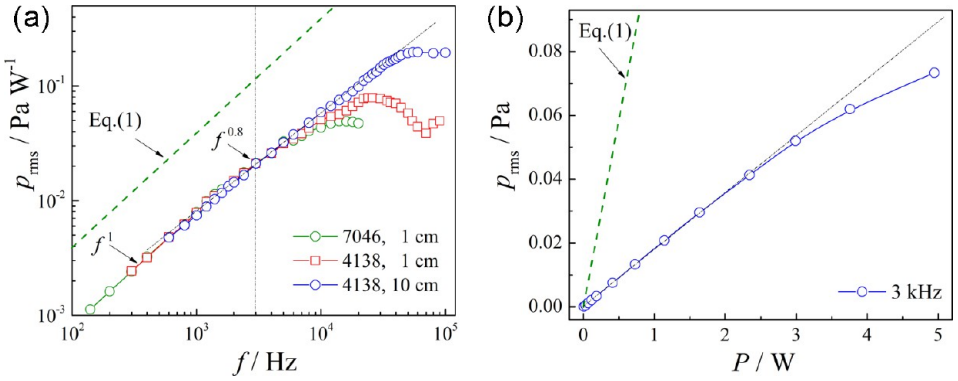

Figure 9. (a) Sound pressure spectra of a gold-coated low-areal-density PAN nanofiber sheet (2.5 × 2.5 cm^2) measured in open air at T_0 = 25 °C for source−microphone distances of r = 1 and 10 cm. The sound pressures are normalized to the applied ac power, P_h = 0.72 W. Open green circles show the $p_{rms}(f)$ response measured using a precision condenser microphone model 7046 (2 Hz to 20 kHz) for a source−microphone distance of 1 cm. The open red squares and open blue circles, measured using microphone model 4138 (6 Hz to 140 kHz), are for 1 and 10 cm distances, respectively. The green dashed line shows the theoretical line calculated using eq 1. (b) Sound pressure *versus* applied ac power for the low-density gold-coated PAN sheet, f = 3 kHz. The temperature on the surface of the heater (measured with infrared camera) for P_h < 5 W did not exceed 35 °C. All plots are normalized to a measurement distance of 3 cm.

of the Au/PAN sheet provides enhanced heat exchange and a broad power range where sound pressure linearly depends on applied power. The $p_{rms}(P_h)$ for the thin sheet shown in Figure 8e (R_0 = 532 Ω) provides a 6-fold lower slope than the theoretical line. However, the linear dependence of $p_{rms}(P_h)$, expanded up to 3 W, demonstrates much better heat exchange with surrounding air than previous sponge samples and the high-areal-density sheet of Figure 8b.

Partial pyrolysis of PAN sheets in inert gases, which preserves the mechanical strength and decreases the fiber diameter, is a promising route to improve the TA performance of the heater. The 3 × 7 cm^2 gold-coated PAN nanofiber sheet shown in Figure 8b, which has a higher density and lower resistance (16 Ω), shows relatively lower performance ($p_{rms} \sim f^{0.6}$). The slope of $p_{rms}(f)$ gradually increases when the gold/PAN sheets undergo partial pyrolysis using resistive heating ($f^{0.6} \rightarrow f^{0.7}$). Surprisingly, at an applied ac current of 0.7 A ($P_h \sim 8$ W), the gold film suddenly evaporated at the bottleneck line (shown in Figure 8c as a gray line) at relatively low temperatures, ~300 °C. Note that while the PAN sheet under the gold coating was partially carbonized, the structure survived. Further study of gold-coated PAN sheets shows a strong tendency for the nanoscale Au film to melt and evaporate at relatively low temperatures on the surface of the TA heater.

Indium−Tin Oxide (ITO)-Coated PAN Sheets. PAN fiber sheets coated with ITO also provide promising results. First, the ITO film can withstand relatively high temperatures in an oxygen environment. Second, these sheets are highly conductive and transparent.

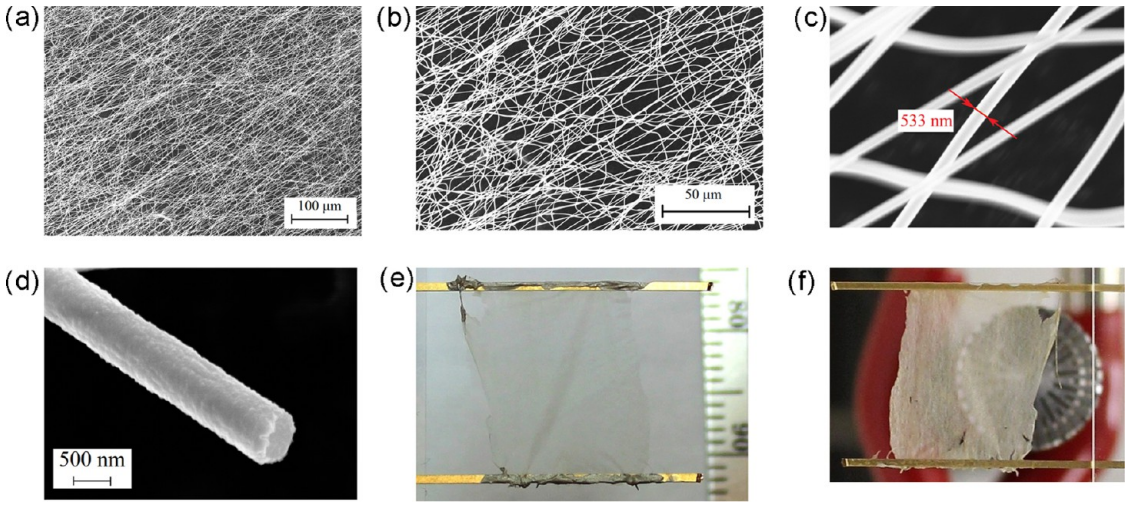

Figure 10. (a−c) SEM images of an ITO-coated PAN nanofiber sheet at different magnifications. (d) SEM image of a hollow ITO tube after being resistively heated in air to burn the PAN core. (e,f) Pictures of a pristine ITO-coated PAN sheet (1.2 × 1.5 cm^2) and the same sheet after the core PAN fibers are burned away (a model 7046 microphone is on the back plane).

Finally, ITO has a positive TCR, which means that short circuiting of the current through a fraction of the coated PAN nanofibers, having higher conductivity, will be mitigated.

The tin-doped indium oxide ($In_{2-y}Sn_yO_{3-\delta}$, $y \sim 0.1$), more commonly known as ITO, was deposited by RF sputtering (1% O_2 in an Ar carrier gas with a flow rate of 12 cm^3 min^{-1} and pressure of 4 mTorr). The thickness of the as-deposited ITO films, estimated from SEM images, varied between 100 and 110 nm. All samples were annealed after deposition in air at 250 °C for 1 h.

The SEM images of Figure 10a−c show the aligned, partially woven structure of ITO-coated PAN fibers, which have an average diameter of ∼400−500 nm and show no trace of bundling. The length of individual fibers is the distance between the pictured electrodes. Therefore, the sheet does not suffer from interconnect resistance, like MWNT sheets that have individual carbon nanotube lengths (250−300 μm) much shorter than the TA projector length. The measured thermal conductivity of individual nanofibers is relatively small (3−4 W m^{-1} K^{-1}) due to the low thermal conductivity of PAN fibers (0.05 W m^{-1} K^{-1}) and the nanoscale thickness of the ITO coating on the PAN nanofibers.

The PAN core can be removed by applying sufficient ac current to burn the PAN in air. Figure 10e,f shows the same sheet before and after core burning. The tubular structure of a resulting ITO fiber is shown in Figure 10d. Despite low electrical conductivity, a single-side-coated PAN sheet demonstrates attractive performance as a TA heater, providing a spectral slope of $\sim f^{0.7}$. Sheets coated on both sides show a reduced spectral slope, $\sim f^{0.53}$, and power dependence of sound pressure (Figure 11a,b). Thus, the increase in the fiber diameter and the thickness of the conductive layer shifts the exponent of sound pressure spectra from 0.7 ($C_h \approx C_p$) to 0.53 ($C_h \approx 6C_p$). This tendency is consistent with the above thermodynamic model of TA transduction (eq 3). More work is needed to reduce the diameter of conductive fibers at least to 50 nm. The open aerogel structure of the ITO/PAN sheets provides excellent heat exchange conditions, resulting in a linear power dependence up to 5 W cm^{-2}, which is close to the power limit of freestanding single MWNT sheets.[18]

The heat capacity of nanostructured materials, which acquire new properties due to the size quantization, cannot be measured in bulk. Here we demonstrate a new simple way to extract the heat capacity of porous nanostructured materials (as it is, without densification or dense packing) from the measured sound spectrum. The red curve in Figure 11 shows a simulation of the sound spectrum of the two-side-coated PAN sheet using the following parameters in eq 3: $T_0 = 300$ K, $\rho_h = 220$ kg m^{-3}, $h = 5$ μm, $r = 3$ cm, $P_h =$ 1 W and, for open ambient air, $\rho_0 = 1.184$ kg m^{-3}, $C_p =$ 1006.3 J kg^{-1} K^{-1}, $\alpha = 22$ mm^2 s^{-1}. The best fitting of this curve with the measured sound pressure data was obtained using $C_h = 600 \pm 6$ J kg^{-1} K^{-1}. The heat capacity estimated from known bulk values for PAN and ITO using the experimentally measured density of pristine and coated sheets, porosity, and sheet thickness gives $C_h = 606$ J kg^{-1} K^{-1} (see S4 in Supporting Information), while the direct experimentally measured heat capacity of the coated sheet pressed into a round-shaped disk ($d = 5$ mm, $h = 1$ mm, $m = 9.927$ mg), using a differential scanning calorimeter (Q2000, TA Instruments Inc.), is 590 J kg^{-1} K^{-1} (see Figure S3 in Supporting Information). The wonderful match of the heat capacity extracted from the sound pressure measurement and direct measurement for this particular sample is due to three factors: (1) The crossover frequency between the two regimes with $C_h > C_p$ and $C_h < C_p$ fell in the frequency region accessible to

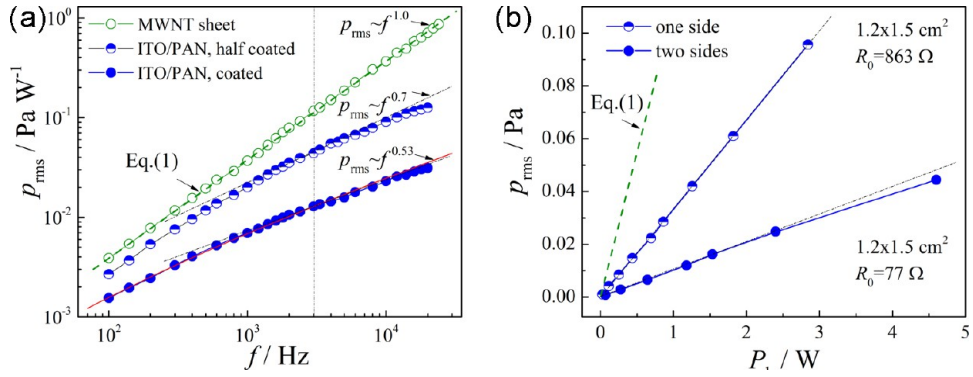

Figure 11. (a) Sound pressure spectrum of the ITO-coated PAN sheet shown in Figure 10e: The half-filled circles are for a single-side-coated sheet (1.2 × 1.5 cm^2, R = 863 Ω, P_h = 0.3 W); the solid circles are for a both-side-coated sheet (1.2 × 1.5 cm^2, R = 77 Ω, P_h = 0.29 W), r = 3 cm. The spectrum of the single-layer MWNT sheet (open circles) (1.5 × 1.5 cm^2, R = 1980 Ω, P_h = 0.24 W) and the theoretical line (green dashed line) are shown for comparison. The linear fits at f = 3 kHz are shown by black dot-dash lines. The red curve shows the simulation of sound spectrum using eq 3 for a both-side-coated sheet. (b) Sound pressure *versus* applied ac power measured at a distance of 3 cm for f = 3 kHz for a single-side (half-filled circles) and both-side-coated sheet (solid circles), respectively.

the used microphones. (2) The heat accumulation in this highly porous aerogel-type ITO/PAN sheet is negligible. (3) The large diameter of PAN fibers and relatively thick ITO coating (80−120 nm) do not substantially affect the phonon spectra. Hence, the heat capacity of the freestanding porous sheet and the bulk pressed mat should be the same. However, in carbon nanotubes, graphene flakes, and other recently studied 2D nanostructures (BN, MoS_2), the heat capacity of individual nanostuctures and their bulk counterparts must be substantially different. Then, the method demonstated above might be useful for estimation of the heat capacity of intact conductive nanostructures. Note that the crossover region for MWNT sheets lies far above the frequency capabilities of these microphones (>140 kHz).

Unlike other sound generation techniques (coil loudspeakers, piezoelectric, magnetostrictive, and electromechanical transducers), the efficiency of TA projectors, η, is proportional to the applied power:[4,5,18]

$$\eta = \frac{\pi \cdot f^2}{\rho_g \upsilon_g C_p^2 T_0^2} P_h \qquad (4)$$

Indeed, since the TA loudspeaker acts as a heat engine, the maximum energy conversion efficiency, according to Carnot's theorem, cannot exceed $\eta = 1 - T_c/T_h$, where T_c is the absolute temperature of the cold reservoir and T_h is the temperature of the hot reservoir. Therefore, high applied power, which implies a high temperature gradient, is a preferable working regime for TA projectors. For T_c = 295 K and T_h = 373 K, the Carnot's efficiency limit is 20%. This efficiency is achievable at high frequencies when thermal and acoustical wavelengths become comparable. For the heaters working in the $C_h < C_p$ regime with low applied ac power, P_h = 1 W (without heat accumulation, so $T_c = T_0$), these conditions are achievable at f > 1 MHz. However, realizing high efficiency at low frequencies is challenging. The applied power should be increased by several orders. Then the thermal stability of the TA heater and heat dissipation from the interior of the heater become a problem, which we address *via* encapsulation of TA heaters in inert gases (argon), structural modification (aerogel porous sheets with $h < 50\ \mu$m), and thermal management of the TA sound projectors.[18]

CONCLUSIONS

Bulk samples of CNT aerogel sheets exhibit fascinating behavior, including highly anisotropic electrical and thermal transport properties and a higher gravimetric strength than the strongest steel sheet. The invention of dry-state technology for the fabrication of freestanding MWNT sheets has resulted in various promising applications. TA sound generation is one of them, which fully exploits the amazing properties of CNTs. However, the limited access to this complex technology is frustrating and hampers the field. Here we have demonstrated several alternative nanostructures that exhibit enhanced TA performance as a heat source with desirable functionality. The sample preparation technologies for these structures are well-established, adequately described in the literature, and can be easily repeated. We have studied the TA performance of these nanostructures as a heat source or as a support for the heat source for TA sound generation. The exponential dependencies of sound pressure on output frequency and input power have been experimentally characterized and compared with theory. Table 2 summarizes the performance and some important thermodynamic parameters of the alternative nanostructures studied in comparison with freestanding MWNT sheets.

While the frequency dependence of sound pressure of the studied nanostructures is explicitly determined by the heat capacity per surface area of the TA heater, the power dependence is more complicated and

TABLE 2. Comparison of TA Sound Source Performance of Alternative Nanostructures at f = 3 kHz, P_h = 1 W

freestanding heater	p_{rms} (Pa)	C_h (J kg^{-1} K^{-1})	ρ (kg m^{-3})	h (μm)	C_h* (J m^{-2} K^{-1})	n
1 CNT sheet	0.117	716(500)[a]	1.0(0.76)	18	13(7.7) $\times$ 10^{-3}	1
2 MWNT forest	0.006	716(500)	32(33.1)	250	5.5(3.8)	0.86
	0.01			80	1.8	0.9
3 MWNT sponge	0.0065	716	30	100	2.15	0.75
	0.012			60	1.3	1
4 graphene sponge	0.051	510−815	2.75	800	1.5	1
5 gold/PAN sheet	0.021	270	494	5	0.66	0.8
6 ITO/PAN sheet half-	0.013	606	220	5	0.68	0.53
deposited	0.044	746	140	5	0.52	0.7

[a] The numbers in parentheses are estimations made in ref 1 using C_h = 500 J kg^{-1} K^{-1}. Measurement and calculation details for the parameters in this table are explained in the Supporting Information.

needs additional thermal analysis. This comprehensive thermal analysis should include separation of the modulated and nonmodulated (accumulated) temperature changes, which could be accomplished through measurement of the third harmonic of current and infrared radiation.[26]

Three-dimensional sponge-type nanostructures, which have the large accessible surface area needed for enhanced heat exchange with the surrounding medium (like thin plates of MWNTs and graphene sponges, including freestanding MWNT forests), demonstrated higher TA performance than their planar-structure counterparts. This can be seen by comparing the sound pressure for the 3D graphene sponge of row 4 in Table 2 (p_{rms} = 0.051 Pa) with that for the planar graphene of row 3 in Table 1 (p_{rms} = 0.0115 Pa). The linear sound pressure spectrum of the graphene sponge, $p_{rms} \propto f^1$, is very close to that of freestanding MWNT forests and indicates that the nanoscale nature of these materials has been preserved, thereby providing a negligible heat capacity of the current-bearing elements.

To avoid heat accumulation inside the heater, which decreases output sound pressure, sufficiently thin plates containing open voids are needed. This plate thickness should be less than the thermal diffusion length (~48 μm for air at 3 kHz). The development of improved tube−tube and graphene flakes interconnects might substantially reduce the sheet resistance of sponge nanostructures and bring them to the desired 8−24 Ω standard values. The negative temperature coefficient of resistance is another drawback of these carbon-based structures, which results in nonuniform current distribution and associated structural failures at relatively low applied power densities (undesired current redistribution burns the aerogel MWNT sheet at P_h = 28 W cm^{-2} in argon). This problem can be mitigated for CNT projectors by deploying single-wall nanotubes that are chirality-selected to have a metallic temperature dependence of electrical conductivity. Similarly, more complete reduction of the reduced graphene sponges (which are made from graphene oxide) can likely be used to realize a metallic temperature dependence of electrical conductivity.

The high reversible compressibility and flexibility that is obtainable for sponge-type TA heaters can be used for the fabrication of complex heater shapes and confined sound sources. This reversible deformability enables the sponge-based TA heaters to conform to surfaces and to be squeezed to fit arbitrarily shaped containers. To obtain optimal TA sound generation conditions, the sponge thickness can be easily adjusted to the thermal diffusion length of the surrounding medium by laser cutting or mechanical compressing the plate between two insulating grids.

While thin plates are preferable for TA sound generation, thick plates appear to be more suitable for sound absorption. The shear viscosity and thermal conduction absorption mechanisms[27] are reinforced in sponge-type nanostructures by deformable air pockets and the high thermal conductivity of individual CNTs and graphene flakes. The high flexibility of individual carbon nanotubes, graphene flakes, and coated PAN nanofibers can substantially enhance the mechanical response to air flow and, consequently, the transfer of the kinetic energy of air molecules to heat.

These thin, flexible, 3D nanostructures can be easily deployed onto curved surfaces to create various desired sound wave profiles. They can simultaneously serve as a TA sound source for active sound cancellation and as a passive sound absorber. Environmentally friendly, mechanically strong, and flexible aerogel TA heaters may be useful for flexible lightweight loudspeakers and SONAR projectors, as well as for devices used for noise cancellation, sound therapy, and acoustic imaging of biosystems.

METHODS

Characterization. The studied nanostructures were characterized by scanning electron microscopy (LEO 1530 VP). The heat capacity at low temperatures (2−350 K) was measured using the heat capacity option of a physical property measurement system (Quantum Design Inc.) and, at high temperatures (200−750 K), using a differential scanning calorimeter (Q2000, TA Instruments Inc.). The temperature on the surface of the samples was measured using infrared thermo-camera T650SC (FLIR System, Inc.) and MobIR (Wuhan Guide Infrared Technology Co., Ltd.).

Acoustic Measurements. The schematic diagram of the setup shown in Figure 12a works as follows: A sinusoidal ac signal of frequency, f, generated by a digital function/arbitrary waveform generator **1** (Agilent 33250A), is amplified by a high-power amplifier **2** and applied to a thermoacoustic projector **3**, which is grounded through a reference resistor (R_{ref} = 1 Ω). Three high-power amplifiers were used for different experimental conditions (2 in Figure 12b): (1) The Trek-PZD350-M/S is a wide-frequency

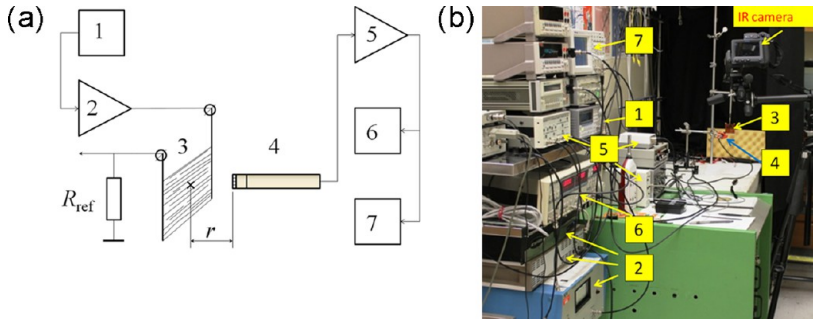

Figure 12. (a) Schematic diagram of the experimental setup, including the ac generator (1), high-power amplifier (2), TA projector (3), a microphone (4) combined with its conditioning amplifier (inside the long tube), a preamplifier (5), a lock-in amplifier (6) for harmonic selection and measurement of the amplitude and phase of the acoustic signal, and a two-channel digital oscilloscope (7) for visualization of the input and acoustical signals. (b) Photograph of the used equipment.

range (dc to 250 kHz) high-voltage (±350 V) piezo-driver amplifier for high impedance projectors (R_0 = 100 Ω to 100 kΩ, output current ±0.4 A). (2) An AE-Techron 8102 power supply amplifier with a frequency bandwidth of dc to 5 kHz and maximum power output ~1100 W was used for low impedance projectors (2−62 Ω). (3) Additionally, we utilized a high-power (100 W), high-frequency (10 kHz to 12 MHz) RF amplifier (model 2100L, Electronics & Innovation, Ltd.). The thermoacoustically generated sound pressure was measured using precision microphones **4** with different apertures *A* and sensitivities *S*: *A* = 12.5 mm for an ACO Pacific model 7046 (2 Hz to 20 kHz, *S* = 54.3 mV/Pa), *A* = 6.25 mm for an ACO Pacific model 7016 (5 Hz to 120 kHz, *S* = 5.43 mV/Pa), and *A* = 3.1 mm for a B&K pressure-field microphone 4138-A-015 (6 Hz to 140 kHz, *S* = 0.543 mV/Pa). The sound pressure level in air was measured using an impulse SPL meter (Quest Technologies, model 2700) provided with a QC-10 acoustic calibrator.

The charge conditioning preamplifier (type 2670 of Bruel & Kjar), which receives the 2*f* acoustical signal *via* the 4138 microphone, amplifies the signal and sends it to another high gain preamplifier "Sound Connect" (Listen Inc.) marked **5**, which increases the detected signal further and sends it to the lock-in amplifier **6** (SR830, Stanford Research Instruments Inc.). The rms amplitude and phase delay of the second harmonic signal are read from the lock-in amplifiers. Simultaneously, the signal goes to a two-channel digital oscilloscope **7** (Tektronix, TDS-210) for visualization of the received signal. The detection of a second harmonic signal using the phase-sensitive lock-in amplifier (**6**) substantially enhances the signal/noise ratio. The reference resistor R_{ref} = 1 Ω is used to control the applied power and dynamic resistance (impedance) of TA projector **3**.

Conflict of Interest: The authors declare no competing financial interest.

Acknowledgment. This research work was supported by Office of Naval Research grants N00014-14-1-0152, Air Force Office of Scientific Research MURI Grant FA9550-12-0035, and Robert A. Welch Foundation Grant AT-0029.

Supporting Information Available: Additional graphs, tables, and calculations. This material is available free of charge *via* the Internet at http://pubs.acs.org.

REFERENCES AND NOTES

1. Xiao, L.; Chen, Z.; Feng, C.; Liu, L.; Bai, Z.-Q.; Wang, Y.; Qian, L.; Zhang, Y.; Li, Q.; Jiang, K.; Fan, S. Flexible, Stretchable, Transparent Carbon Nanotube Thin Film Loudspeakers. *Nano Lett.* **2008**, *8*, 4539–4545.
2. Aliev, A. E.; Lima, M. D.; Fang, S.; Baughman, R. H. Underwater Sound Generation Using Carbon Nanotube Projectors. *Nano Lett.* **2010**, *10*, 2374–2380.
3. Xiao, L.; Liu, P.; Liu, L.; Li, Q.; Feng, Zh.; Fan, Sh.; Jiang, K. High Frequency Response of Carbon Nanotube Thin Film Speaker in Gases. *J. Appl. Phys.* **2011**, *110*, 084311–084315.
4. Aliev, A. E.; Gartstein, Y. N.; Baughman, R. H. Increasing the Efficiency of Thermoacoustic Carbon Nanotube Sound Projectors. *Nanotechnology* **2013**, *24*, 235501.
5. Vesterinen, V.; Niskanen, A. O.; Hassel, J.; Helistö, P. Fundamental Efficiency of Nanothermophones: Modeling and Experiments. *Nano Lett.* **2010**, *10*, 5020–5024.
6. Tong, L. H.; Lim, C. W.; Li, Y. C. Gas-Filled Encapsulated Thermal-Acoustic Transducer. *J. Vib. Acoust.* **2013**, *135*, 051033.
7. Tian, H.; Ren, T.-L.; Xie, D.; Wang, Y.-F.; Zhou, C.-J.; Feng, T.-T.; Fu, D.; Yang, Y.; Peng, P.-G.; Wang, L.-G.; Liu, L.-T. Graphene-on-Paper Sound Source Devices. *ACS Nano* **2011**, *5*, 4878–4885.
8. Suk, J. W.; Kirk, K.; Hao, Y.; Hall, N. A.; Ruoff, R. S. Thermoacoustic Sound Generation from Monolayer Graphene for Transparent and Flexible Sound Sources. *Adv. Mater.* **2012**, *24*, 6342–6347.
9. Tian, H.; Xie, D.; Yang, Y.; Ren, T.-L.; Feng, T.-T.; Wang, Y.-F.; Zhou, C.-J.; Peng, P.-G.; Wang, L.-G.; Liu, L.-T. Poly(3,4-ethylenedioxythiophene):Poly(styrenesulfonate)-Based Organic, Ultrathin, and Transparent Sound-Emitting Device. *Appl. Phys. Lett.* **2011**, *99*, 233503.
10. Tian, H.; Xie, D.; Yang, Y.; Ren, T.-L.; Wang, Y.-F.; Zhou, C.-J.; Peng, P.-G.; Wang, L.-G.; Liu, L.-T. Transparent, Flexible, Ultrathin Sound Source Devices Using Indium Tin Oxide Films. *Appl. Phys. Lett.* **2011**, *99*, 043503.
11. Shinoda, H.; Nakajima, T.; Ueno, K.; Koshida, N. Thermally Induced Ultrasonic Emission from Porous Silicon. *Nature* **1999**, *400*, 853–855.
12. Niskanen, A. O.; Hassel, J.; Tikander, M.; Maijala, P.; Grönberg, L.; Helistö, P. Suspended Metal Wire Array as a Thermoacoustic Sound Source. *Appl. Phys. Lett.* **2009**, *95*, 163102.
13. Zhang, M.; Fang, S. L.; Zakhidov, A. A.; Lee, S. B.; Aliev, A. E.; Williams, C. D.; Atkinson, K. R.; Baughman, R. H. Strong, Transparent, Multifunctional, Carbon Nanotube Sheets. *Science* **2005**, *19*, 1215–1219.
14. Chitnis, G.; Kim, A.; Song, S. H.; Jessop, A. M.; Bolton, J. S.; Ziaie, B. A Thermophone on Porous Polymeric Substrate. *Appl. Phys. Lett.* **2012**, *101*, 021911.
15. Sugimoto, T.; Nakajima, Y. Acoustic Characteristics of a Flexible Sound Generator Based on Thermoacoustic Effect. *IEEE. Sens. J.* **2013**, *19*, 030004.
16. Arnold, H. D.; Crandall, I. B. The Thermophone as a Precision Source of Sound. *Phys. Rev.* **1917**, *10*, 22–38.
17. Hu, H.; Wang, Z.; Wu, H.; Wang, Y. Analysis of Spherical Thermoacoustic Radiation in Gas. *AIP Adv.* **2012**, *2*, 032106.
18. Aliev, A. E.; Mayo, N. K.; Baughman, R. H.; Avirovik, D.; Priya, S.; Zarnetske, M. R.; Blottman, J. B. Thermal Management of Thermoacoustic Sound Projectors Using a Free-Standing Carbon Nanotube Aerogel Sheet as a Heat Source. *Nanotechnology* **2014**, *25*, 405704.
19. Kozlov, M. E.; Haines, C. S.; Oh, J.; Lima, M. D.; Fang, S. Sound of Carbon Nanotube Assemblies. *J. Appl. Phys.* **2009**, *106*, 124311.
20. Singh, D. K.; Iyer, P. K.; Giri, P. K. Diameter Dependence of Oxidative Stability in Multiwalled Carbon Nanotubes: Role

of Defects and Effect of Vacuum Annealing. *J. Appl. Phys.* **2010**, *108*, 084313.
21. Cui, Y.; Zhang, M. Fabrication of Cross-Linked Carbon Nanotube Foam Using Polymethylmethacrylate Microspheres as Templates. *J. Mater. Chem. A* **2013**, *1*, 13984–13988.
22. Jiang, L.; Fan, Zh. Design of Advanced Porous Graphene Materials: From Graphene Nanomesh to 3D Architectures. *Nanoscale* **2014**, *6*, 1922–1945.
23. Bi, H.; Yin, K.; Xie, X.; Zhou, Y.; Wan, N.; Xu, F.; Banhart, F.; Sun, L.; Ruoff, R. S. Low Temperature Casting of Graphene with High Compressive Strength. *Adv. Mater.* **2012**, *24*, 5124–5129.
24. Zhang, L.; Zhang, F.; Yang, X.; Long, G.; Wu, Y.; Zhang, T.; Leng, K.; Huang, Y.; Ma, Y.; Yu, A.; Chen, Y. Porous 3D Graphene-Based Bulk Materials with Exceptional High Surface Area and Excellent Conductivity for Supercapacitors. *Sci. Rep.* **2013**, *3*, 1408.
25. Rahaman, M. S. A.; Ismail, A. F.; Mustafa, A. A. A Review of Heat Treatment on Polyacrylonitrile Fiber. *Polym. Degrad. Stab.* **2007**, *92*, 1421–1432.
26. Aliev, A. E.; Gartstein, Y. N.; Baughman, R. H. Mirage Effect from Thermally Modulated Transparent Carbon Nanotube Sheets. *Nanotechnology* **2011**, *22*, 435704.
27. *Properties of Gases, Liquids, and Solutions: Principles and Methods*, Part 1; Warren, P., Ed.; Academic Press: New York, 2013; Vol. 2, p 494.